Research Square

Preprints are preliminary reports that have not undergone peer review.
They should not be considered conclusive, used to inform clinical practice,
or referenced by the media as validated information.

What the line delivers: a physics-guided design platform for time-modulated transmission lines

Aiganym Abzaliyeva
Nazarbayev University
Constantinos Valagiannopoulos
National Technical University of Athens
Bakhtiyar Orazbayev
bakhtiyar.orazbayev@nu.edu.kz

Nazarbayev University

Article

Keywords:

Posted Date: November 18th, 2026

DOI: https://doi.org/10.21203/rs.3.rs-11565776/v1

License: This work is licensed under a Creative Commons Attribution 4.0 International License.
Read Full License

Additional Declarations: No competing interests reported.

What the line delivers: a physics-guided design platform for time-modulated transmission lines

Aiganym Abzaliyeva[1], Constantinos Valagiannopoulos[2], and Bakhtiyar Orazbayev[1,*]

[1]Department of Physics, Nazarbayev University, Astana, Kazakhstan
[2]School of Electrical and Computer Engineering, National Technical University of Athens, Athens, Greece
[*]Corresponding author: bakhtiyar.orazbayev@nu.edu.kz, aiganym.abzaliyeva@nu.edu.kz

Abstract

Time-varying transmission lines offer rich signal control and a testbed for diverse wave phenomena. However, theory usually prescribes the modulation, whereas in hardware it is set by the pump reaching each modulated element—a delivery step rarely made explicit. We therefore present a physics-guided platform that links cross-validated Floquet and harmonic-ABCD analysis, inverse design, circuit harmonic balance, full-wave simulation, and measurements for line-fed packaged varactors on shunt stubs. Its pump-delivery rule predicts that delivery–transport competition narrows the admissible design space as pump frequency and varactor susceptance increase. Our platform quickly selects candidates before any nonlinear simulation, using model-based screening that combines junction transfer, pump and signal transport, and geometric constraints. As a demonstration, it delivered a varactor-loaded design with absolute signal gain in harmonic-balance simulation, with the analytical prediction and the harmonic-balance certification in close agreement. For a separate, previously fabricated 20-cell microstrip line, the platform predicts starved-pump delivery while the measured two-tone controls for the line do not establish amplification of the injected signal under the tested conditions. The platform thus provides a reproducible, versatile workflow for practical time-varying device design, expanding the tools available for testing wave phenomena in transmission lines.

Keywords: time-varying transmission lines; time-modulated media; parametric amplification; design platform; pump delivery; Floquet analysis; open-source toolchain

Introduction

Engineering media whose constitutive parameters vary in time adds a powerful degree of freedom to electromagnetic design, beyond what spatial structuring alone can reach. Modulating permittivity, permeability, or lumped circuit elements in time redistributes energy among frequency harmonics, can break time-reversal symmetry, and adds parametric routes, besides static gain and loss, to non-Hermitian regimes[1–5,22]. Moreover, momentum bandgaps of temporal and spatiotemporal crystals host exponentially growing rather than propagating states, suggesting compact amplifiers, nonreciprocal components, and waveform shapers driven by a modulation tone instead of magnets or transistor gain stages[6–8,23]. Transmission lines (TLs), the building blocks of RF and mm-wave circuits, are a natural platform for these ideas. Spatiotemporally modulated TLs have already produced magnetless isolators, circulators, and nonreciprocal filters[9–13], building on classical analyses of dispersion in space–time-periodic media[14,15] and on time-domain numerical methods[16–20].

Time-varying TLs (TVTLs) can also act as parametric amplifiers in which a pump at $f_p = 2f_s$ feed the degenerate signal–idler pair[21,24]. When the pump co-propagates with the signal along the nonlinear line itself, the device is the classical traveling-wave parametric amplifier (TWPA) of the late 1950s[25–27], whose intrinsic limit Landauer traced to the phase-matched harmonic cascade[28]. Sixty years later, the idea has triumphed where loss is nearly absent. Kinetic-inductance

and Josephson TWPAs, including dispersion-engineered photonic-crystal designs, routinely deliver ∼20 dB near the quantum limit at millikelvin temperatures[29–31]. At room temperature, in printed circuits, the same lineage has had a more modest career. For instance, works of Kozyrev and van der Weide demonstrated parametric amplification above 10 dB together with a rich harmonic phenomenology[32,33], and related effects appear in electrical lattices supporting driven localized modes[38], magnetically tuned nonlinear metamaterials[39], distributed CMOS parametric dividers[40], and distributedly modulated capacitor (DMC) lines used as nonreciprocal notch amplifiers[10,11]. A microstrip varactor TVTL in the non-degenerate regime achieved a 2.43 dB insertion-loss improvement[41].

Recent experiments have demonstrated alternative approaches to achieving effective temporal modulation. Modulated microwave lines exhibit photonic time-crystal momentum bandgaps and temporal amplification[42,43]. Optical modulation of distributed photodiodes has demonstrated positive terminal gain in a microwave time-crystal line[44]. Parametric metasurfaces have also shown promising results, progressing from theoretical predictions of amplified frequency conversion[45] to experimental demonstrations using varactor loaded structures[46]. In parallel, temporal non-Foster systems have been proposed for wave confinement and amplification through active material responses[47]. However, these approaches differ in their excitation mechanisms and gain definitions, making their reported enhancements distinct from the absolute input-to-output transmission measured at the connectors of a transmission line pumped through the line itself. They also sharpen the question a self-fed line cannot avoid: how much of the prescribed modulation actually reaches the element it is meant to modulate.

Here, to answer this question, we derive a pump-delivery rule by considering a microstrip line periodically loaded with packaged varactors on shunt stubs, with signal and pump injected through one port. The pump must propagate through the loaded line and divide across the package, junction, and stub impedances. Consequently, a modulation depth prescribed in an ideal time-varying model need not be available at a physical junction. A useful design workflow must keep this delivery problem explicit while connecting geometry, linear response, nonlinear circuit calculations, and experimental evidence.

To address this challenge, we develop a unified design platform based on a Floquet and harmonic ABCD formulation, supported by circuit and full-wave simulations. The framework combines inverse design to identify geometries that meet prescribed targets with forward analysis to evaluate their performance. A three-condition pump delivery criterion accounts for branch transfer, pump propagation, and signal propagation, alongside geometric feasibility. The resulting thresholds apply to the specified model and excitation assumptions rather than imposing universal limits on parametric gain. As an independent benchmark, we examine Cui et al.[48], who demonstrated parametric amplification in a varactor-loaded printed spoof plasmon transmission line pumped through the line itself. Their results provide an external reference for evaluating the proposed framework in the Discussion.

We first apply the platform to the fabricated transmission line comprising 20 unit cells with varactor-loaded stubs. Under the investigated conditions, the predicted pump voltage delivered to the varactors remains well below the required threshold, while experimental two-tone measurements do not establish amplification of the injected signal under the tested conditions. We then demonstrate the framework's practical potential using an alternative simulated design with SMV2019 varactors, 40 cells, and an operating frequency of $f_s = 1.26$ GHz at 8.7 V bias, for which harmonic balance records an absolute out/in of +6.3 dB at the best sampled pump phase (degenerate) and +20 dBm pump, certified by finite-duration checks.

Previous studies have addressed pump coupling and modulation depth through varactor voltage division[34], Josephson amplifier pump port synthesis[35], and experimental measurements of delivered pump strength[46]. The sequence of linear design followed by nonlinear verification has also been explored for artificial transmission lines[36]. Building on these advances, we establish a unified design criterion that captures the competing effects of pump transfer to the varactor junction, pump and signal propagation, and geometric feasibility. By explicitly accounting for

the interaction between branch reactance and pump transport, the framework enables systematic screening of candidate geometries while distinguishing analytical predictions, circuit simulations, and experimental evidence. This approach provides a reproducible alternative to conventional trial-and-error design, supported by comparison with an independently reported parametric amplifier.

Results

The design problem and the platform

Figure 1a summarizes the proposed platform. A design is specified by its target (f_s, $f_p = 2f_s$, the varactor and its bias, the board dimensions) and screened against four criteria before any nonlinear simulation: delivery of the pump to the junction (A), transport of the pump along the line (B), buildability (fabrication feasibility on the board) (C), and transport of the signal (D). Candidates that pass are verified by models—the analytical Floquet/harmonic-ABCD core, circuit-level harmonic balance, and full-wave simulation of the unit cell—and, for the fabricated line, compared with VNA and two-tone measurements (Methods). The device itself is a microstrip line with N periodic cells, each loaded with a varactor on a shunt stub (Fig. 1b). Signal and pump enter through one port, so the pump must first propagate along the periodically loaded line following its Bloch dispersion and then pass through the stub and package to reach the junction (Fig. 2a). The same geometry therefore sets three coupled resonances at once—dispersion, modulation depth at the junction, and nonlinear transmission—and the platform runs in both directions: inverse design screens candidates against (A–D), forward analysis evaluates a chosen one.

Analytical model and the pump-delivery rule

The central design question for a TVTL is not simply whether the pump propagates, but how much of it arrives where modulation takes place. The relevant quantities are therefore the pump attenuation per cell and the voltage transferred to the junction, both of which follow from the ABCD model of a single unit cell. The complete TVTL is treated as a cascade of identical unit cells, each described by its own cell matrix. Each cell is modeled as a T-network consisting of two series microstrip sections of length $p/2$, which form the arms of the T, and a central shunt branch that contains the time-varying element. The ABCD matrix of each section is derived separately, and the response of the whole cell is obtained by multiplying these matrices in sequence. This approach provides a compact, systematic description of the line and forms the basis for the design screening that follows. The full derivation of the approach is shown in the Methods.

In Methods, the junction is described by its elastance $S = 1/C$, which makes the charge dynamics linear with periodic coefficients and leads to a Floquet chain of harmonics; its key prediction is a single bounded gain lobe with maximum and minimum 180° apart in pump phase (Supplementary Section S2). The elastance form is convenient for the derivation, whereas the numerical core is evaluated in the equivalent capacitance form, $C(t) = C_0[1 + m\cos(\omega_p t)]$, which connects directly to the varactor's capacitance-voltage data. Both forms also share the same relative slope, $k = |d\ln C/dV| = |d\ln S/dV|$. The results below therefore do not depend on which form is used. The slope also connects delivery and modulation. A pump of amplitude V_{bt} at the top of the branch produces the junction depth

$$m_j = k\,T\,V_{\mathrm{bt}}. \tag{1}$$

The transport α, the transfer T and the required depth now define the conditions that candidate design should fulfill. For a given branch model, the design meets the electrical requirements only if

$$\text{(A)}\ \ T(f_p) \geq T_{\mathrm{req}}, \qquad \text{(B)}\ \ \alpha(f_p) \leq \alpha_{\max}, \qquad \text{(D)}\ \ \alpha(f_s) \leq \alpha_{\max}. \tag{2}$$

Condition (A) requires sufficient pump voltage at the junction, while (B) and (D) limit the attenuation of the pump and the signal along the line. A fourth, geometric criterion (C) requires the design to be buildable. The stub must fit within the per-cell slot of the 150×30 mm design envelope, and the N-cell cascade within its length ($Np \leq 150$ mm).

Figure 2b,c shows the two conditions for the certified design and the as-built line (Methods). The dashed curve also shows where the line lets the pump through. It stays close to 0 dB in the passbands, where the pump propagates, and drops sharply in the stopbands, where it cannot. A simpler design rule would only ask whether the pump lies in a passband. Condition (B) is deliberately stricter, because a wave inside a passband may still lose much of its power over many cells. For example, a circuit simulation in ADS of a frequency window that passes the passband check alone gives a pump-on/off ratio of only +0.002 dB, so the pump has almost no effect there (Supplementary Section S3). A quantitative limit on the attenuation, here $\alpha_{\max} = 0.02$ Np/cell, excludes such cases, and condition (D) applies the same limit to the signal. The delivery threshold $T_{\mathrm{req}} = 0.174$ is also a chosen value rather than a universal constant.

Each condition can be met on its own. The difficulty is that conditions (A) and (B) depend on the same branch impedance but require opposite values of it. Delivery is large when the stub cancels most of the varactor reactance, so that the branch impedance becomes small, whereas transport requires a large branch impedance, so that the branch loads the line only lightly. A branch that lets the pump through to the junction (large T) also loads the line strongly, which raises the pump attenuation (large α). Delivery and transport therefore compete, and Fig. 2b,c shows this directly. In both panels, the peaks of the delivery curve fall where the transport curve drops into a stopband. For the fabricated line (Fig. 2c), the delivery exceeds its threshold only below about 3 GHz and around its peak near 10.5 GHz, and in both ranges the pump cannot propagate. In the passband between them, the delivery falls far below its threshold, with a deep minimum near 6.4 GHz. The two conditions are therefore never met together. For the certified design (Fig. 2b), the delivery peaks near 1.5 and 3.2 GHz also coincide with stopbands, but between them the delivery stays well above its threshold while the pump loss stays within its limit. Both conditions are therefore met over wide frequency ranges (green bars), and the operating point at $f_s = 1.26$ GHz lies within one of them.

In a reduced model, the cell is represented by a transmission line of impedance Z_0 loaded by a lossless branch of reactance X (Supplementary Section S3). In this model, the range of unloaded phase shifts per cell, $\vartheta = \beta_0 p$, that satisfy both (A) and (B) is governed by a single parameter,

$$u_{\min} \;=\; \tfrac{1}{2}\, Z_0\, T_{\mathrm{req}}\, \omega_p C_0, \tag{3}$$

which is the pump susceptance of the varactor, $\omega_p C_0$ with $C_0 = C_j + C_P$, normalized to the line admittance. The larger $u_{\min}$, the fewer phase shifts ϑ satisfy both conditions, so increasing the varactor capacitance or the pump frequency steadily reduces the number of working designs. Figure 2d tests this scaling with the full model. Its horizontal axis is the pump loading $\omega_p C_0 Z_0$, which measures how strongly the varactor loads the line at the pump frequency and is proportional to $u_{\min}$. Each blue curve corresponds to one junction capacitance (0.3, 1, 3 and 7.37 pF), and each point on a curve to one pump frequency between 2 and 16 GHz. At that frequency, stubs with lengths from 0.4 to 3.0 times the as-built stub are tested against conditions (A) and (B), and the point gives the percentage that pass both. The grey dashed curve is the closed-form estimate of Eq. (3) for a lossless line, which checks delivery only. Both follow the same trend. The percentage of passing stub lengths reaches about 90 % for 0.3 pF at light loading, stays below 20 % for 3 pF, and is zero over the whole range for the 7.37 pF part used on the board. The certified design lies at a pump loading of about 0.37, where many stub lengths pass, whereas the as-built line lies at about 14.4, where none pass. A smaller junction capacitance or a lower pump frequency are therefore the most effective ways to obtain a working design.

Time-domain companion: the assumption, the cascade, and its escape

To study the effect of pump delivery on amplification along a complete line, a finite-difference time-domain (FDTD) companion model is used (Fig. 2e,f). The model describes an idealized RLCG line, so its results illustrate the general physics rather than predict a specific device. The FDTD companion details are shown in the Methods and Supplementary Materials.

The FDTD companion model first compares the standard assumption of time-varying media theory with a pump that is carried by the line itself. Fig. 2e shows the pump-on/off ratio of the signal as a function of line length, measured in signal wavelengths λ_0. When the modulation is prescribed uniformly, with the same depth m everywhere along the line (blue curve), the ratio grows steadily with length and reaches +15 dB at $4\lambda_0$ for $m = 0.25$. The picture changes markedly when an in-band pump wave at $2f_s$ instead produces the modulation and travels along the line with the signal. Even with full delivery ($T = 1$) and at the best pump phase (red dashed curve), the ratio never exceeds +2.09 dB, and at less favorable phases the signal is attenuated rather than amplified (grey shading). With strongly reduced delivery ($T = 0.05$), as expected for a typical commercial varactor, the ratio remains below +0.2 dB (dash-dotted curve).

The traveling pump performs poorly even at perfect delivery because of the phase-matched up-conversion cascade identified by Landauer[28]. On a smooth line, the amplified signal transfers its energy coherently to the harmonics at $3f_s$ and $5f_s$. Figure 2f makes this loss visible by comparing the output levels at f_s, $3f_s$ and $5f_s$, relative to the pump-off signal, for the in-band pump at its best phase and a line length of three wavelengths. On the ordinary smooth line (hatched bars), the $3f_s$ harmonic grows by +3.4 dB, more than the signal itself, which gains only about +1.9 dB. Periodic loading can block this loss. In a Bloch-dispersive line whose stopband contains $3f_s$, waves at this frequency cannot propagate, while the pump remains matched to the loaded line (blue bars). The $3f_s$ harmonic then drops to −1.7 dB, and the signal rises to +7.48 dB. This is the same dispersion-based escape that left-handed lines[32,33] and photonic-crystal TWPAs[31] exploit.

Two conditions therefore emerge for amplification in a line that carries its own pump. The pump must reach the junctions, and the line's dispersion must suppress the up-conversion cascade. The fabricated line directly tests the first condition.

The fabricated line: pump-off response and delivery diagnosis

Figure 3a shows the fabricated board and an enlarged view of its unit cell. The line contains 20 cells loaded with unbiased SMV1245 varactors on RO4003C. Each cell follows the T-network of the analytical model with two series microstrip arms and a shunt branch, in which the varactor is in series with stepped stub sections. The period is $p = 6.11$ mm and the main-line width is $w = 4.27$ mm, and each stub is grounded through two 0.8 mm holes (dimensions in Supplementary Table S7).

Before the delivery rule is applied, the passive model must be compared with the board. Figure 3b compares the transmission $|S_{21}|$ measured by VNA with the predictions of four models of increasing detail, such as the analytical ABCD model, the ADS circuit model, ADS Momentum co-simulation and COMSOL full-wave simulation. At the signal frequency $f_s = 3.1$ GHz, the agreement is good, with the models giving −1.3 to −2.4 dB against a measured −2.0 dB. At the pump frequency of 6.2 GHz, however, the models give −0.5 to −1.6 dB, whereas the measurement drops to −11.0 dB, at the edge of a stopband that none of the models predicts. This discrepancy remains unresolved (Discussion), so the comparison does not validate the models at the pump frequency. The near-field scan provides an independent check of the dispersion (Fig. 3c). From the measured field along the line, the pump phase mismatch per cell at 3.1 GHz is 24.8°, close to the 26.1° predicted for the analytical cell.

With these reservations in mind, the delivery rule clearly predicts the board. At $f_s = 3.1$ GHz ($f_p = 6.2$ GHz), the branch transfer is only $T = 0.0026$, about 67 times below the delivery threshold, because the pump frequency falls close to the delivery minimum of the branch at 6.42 GHz (Fig. 2c). Transport, by contrast, is not the limiting factor, since the modelled Bloch

attenuation amounts to only about -0.4 dB over the 20 cells at the pump frequency. The board therefore fails condition (A) but not condition (B). In other words, the pump propagates along the line but does not reach the junctions. Near $f_s = 5.3$ GHz, the situation is reversed. Here the branch transfer exceeds the threshold by a factor of 2.7, but the pump is strongly attenuated, with $\alpha(10.6\,\mathrm{GHz}) = 1.80$ Np/cell. The two operating points thus fail for opposite reasons, as expected from the competition between delivery and transport.

Parametric measurements

Two-tone measurements were used to check whether any amplification occurs when pump signal reaches the junctions (Fig. 3d). Signal and pump are combined in a directional coupler and injected through the single input port, the transmitted spectrum is recorded at the output (Fig. 3d). Each measurement is repeated with a through connection in place of the device to separate the line response from the measurement setup. The levels are read directly at the analyzer without calibration. Comparing them therefore assumes that the analyzer responds linearly while the strong pump is present, which was not verified.

Figure 3d shows four spectra around $f_s = 3.1$ GHz, with the pump at 6.2 GHz. Without the pump, the signal appears as a clear line (blue). With the pump switched on, a line at f_s appears even when no signal is injected (red dashed). Adding the signal raises this line by only $+0.23$ dB (red solid). A line at f_s also appears when the device is removed and only the pump is applied (grey dotted), so it is produced by the measurement chain rather than by the line. A line at f_s in the pump-on spectrum is therefore not, by itself, evidence of amplification. The same test was repeated at 11 further frequencies in three bands. In all cases, adding the signal changes the line at f_s by -2.3 to $+1.2$ dB, within the range expected for a signal that is not amplified (Supplementary Fig. S15 and Section S6).

Under the tested conditions, the two-tone controls do not establish amplification of the injected signal. Independently, the delivery rule places the delivered pump far below threshold. Whether a line that passes the rule does amplify is the question of the next section.

From rule to design: screening and the certified record

The delivery diagnosis first shows how far the fabricated line is from gain. At $f_s = 3.1$ GHz with $N = 20$, a +1 dB pump on/off ratio, corresponding to an absolute input to output transmission of -7.1 dB, requires a uniform modulation depth $m = 0.108$ under ideal phase matching. However, the delivered depth at +19.5 dBm is only 0.0019 to 0.0022. With the actual pump phase, the target remains unattainable even at $m = 0.6$ (Supplementary Fig. S13). The formal signal and idler exceptional points occur at $m = 8.96$ for the screening cell and $m = 3.99$ for the ridge derived mismatch (Supplementary Fig. S4a). These values beyond $m = 1$ quantify the mismatch rather than define thresholds for finite gain (Supplementary Section S2).

The rule also shows that this gap cannot be closed by reshaping the stub alone. Figure 4c compares the buildable stub lengths with those satisfying criteria A, B, and D for the unbiased SMV1245. The as-built stub is 13.1 mm long, within the buildable limit of 22.2 mm ($s = 1.689$). However, admissible designs require $s = 3.95$ to 5.70, corresponding to stub lengths of 51.8 to 74.8 mm at $f_s = 1.0$ to 1.4 GHz. Thus, no buildable window exists within the scanned geometry, pump band of 2 to 16 GHz, scale range, and attenuation limits. The alternative stub model gives the same conclusion, with unbiased windows only at $s \geq 3.9$ for $f_s = 0.95$ to 1.40 GHz and below 0.3 GHz (Supplementary Fig. S5). Reverse bias reduces C_0 and restores some buildable windows (Fig. 4d). With 1–5 V, buildable cells meet criteria A, B and D mostly below about 0.7 GHz and at isolated points between 3 and 4.4 GHz, whereas the as-built design remains outside them. Importantly, admissibility does not guarantee gain. At 3.05 GHz, $s = 1.6$, and 3 V, an admissible cell produces only -0.6 dB absolute transmission at +10 dBm (Supplementary Table S3).

Applied before nonlinear simulation, the screening rule becomes a practical design tool (Fig. 4a,b). Rerun within the 150×30 mm envelope with $N_{\mathrm{model}} = 15$ at $f_s = 3.1$ GHz, it first reproduces the

verdict for the as-built part (Fig. 4a). None of the 2,034 evaluable designs passes A, B, and C, identically for every $N_{\mathrm{model}} = 9$–21 (the criteria are per cell) and also in a separate $f_s = 2$–$6\,\mathrm{GHz}$ sweep of the as-built geometry. The mechanism is the competition derived above. The points form a band that turns upward before reaching sufficient delivery, so no design satisfies both (A) and (B) ($\mathrm{A} \wedge \mathrm{B} = 0$), and the two quantities are strongly correlated, with $\mathrm{corr}(\log T, \log \alpha) = +0.883$. Had the criteria been statistically independent, approximately 125 designs would have passed (A), (B) and (C) together ($n_{\mathrm{A}} n_{\mathrm{B}} n_{\mathrm{C}} / n^2$), whereas the falsified passband criterion would have admitted 61 (28 with buildability). Both counts refer to the earlier screening threshold of the scan (Methods). The picture changes once the part is chosen by the $\omega_p C_0$ scaling of Eq. (3) (Fig. 4b). For the SMV2019 at 20 V, $\omega_p C_0 = 8.8\,\mathrm{mS}$, against 287 mS for the as-built SMV1245 at 0 V ($f_p = 6.2\,\mathrm{GHz}$). The band therefore shifts to higher delivery and crosses the admissible region, and 781 of 3,083 evaluable designs (25.3 %) pass A, B and C, both counts being drawn from the same 3,245 candidates.

Nevertheless, passing the screen does not ensure amplification, and signal transport remains essential. Supplementary Fig. S17 compares a misleading candidate with a separately optimized record, then evaluates both by harmonic balance. The designs differ in bias, cell number, frequency, cell model, and excitation. The misleading candidate satisfies A, B, and C but fails D at the earlier threshold $T_{\mathrm{req}} = 0.1438$. At $f_s = 3.1$ GHz and +35 dBm pump power through a single $50\,\Omega$ port, it shows a +15.6 dB pump on/off ratio but an absolute transmission of −25.5 dB and a 104 dB analytical discrepancy. This demonstrates why relative gain must always be reported alongside absolute transmission.

The certified design (Fig. 5) satisfies both time-domain conditions. It is a 40-cell SMV2019 line at $f_s = 1.26\,\mathrm{GHz}$ and 8.7 V bias, built from electromagnetically modeled unit cells. It passes delivery, pump transport, and signal transport (A, B, D) with margins of 17, 1.6, and 5.4 dB, and its delivery and transport curves overlap over a wide band around the operating pump frequency (Fig. 2b). At about 237 mm, it exceeds the length of the 150×30 mm envelope, which is a design choice rather than the outline of the fabricated board, so we did not apply criterion (C). Its dispersion provides the escape from the cascade: the pump stays on the phase-matching line ($\Delta\theta = -0.3°$ per cell), whereas up-conversion to $3f_s$ is mismatched by 14° per cell (Fig. 5a). The pump is also delivered as predicted: its amplitude at the junctions falls by 5.3 dB over 40 cells, within the 6.95 dB limit of criterion B, and the analytical and harmonic-balance values agree within 2.1 % (Fig. 5b). In harmonic balance, the line reaches an absolute out/in of +6.3 dB at the best sampled pump phase (270°) and +20 dBm pump (+7.9 dB pump-on/off ratio, pump-off −1.6 dB; non-degenerate check: Supplementary Table S2), and the gain region extends over a range of pump phases and powers (Fig. 5c). The analytical core predicts the peak within 0.09 dB, and within 2.39 dB away from it (Fig. 5d).

To confirm that this design behaves as a stable amplifier, we checked the record against the certification criteria (Methods). Its phase response forms a single bounded lobe, as predicted by the analytical core, with extrema at 270° and 90°, separated by 180° (Fig. 5d). With the signal switched off, the output almost vanishes ($r_A = 0.001$), and the output grows in proportion to the input signal (slope 1.00). The response stays bounded for pump powers from +11 to +23 dBm, the junction voltages remain within the 22 V rating, and the results do not change when the harmonic order is raised from 5 to 9 (within 0.05 dB).Across eight tolerance corners, the absolute out/in stays between 5.8 and 6.7 dB. The record also passes the stability protocol at all nine points. Without the signal, the output stays below −80 dBm. Over about 590 pump periods (234 ns), no growing transient appears, either at the operating pump power or 2 dB above it. The pump power can be raised by 7.0–7.5 dB above the operating level before a junction reaches its reverse voltage rating. These checks cover a finite time and a finite set of conditions, so they do not prove stability for unlimited time, and the voltage margin is a model value rather than a measured one. The record is a simulation, not a measurement of the fabricated prototype, and it is included in the data deposit.

Together, these results establish two requirements for varactor selection. First, the pump

loading $\omega_p C_0$ must be sufficiently low to satisfy delivery and transport constraints. Second, the varactor must provide adequate modulation depth per unit pump voltage, expressed as

$$\left|\frac{C'}{C}\right| = \frac{M}{V_J + V}\,\frac{C_j}{C_j + C_P}, \tag{4}$$

The first factor depends on the junction grading coefficient M and bias voltage rather than junction size, indicating that reducing junction capacitance does not necessarily reduce modulation depth per volt. However, the second factor shows that package capacitance C_P weakens modulation, particularly as junction capacitance C_j decreases (Supplementary Section S5).

Discussion

The central challenge in time-modulated transmission lines is not merely generating parametric modulation but ensuring sufficient pump delivery to each nonlinear element. The pump must propagate through a lossy and dispersive lattice and reach the varactor junction through the stub and package. Our framework addresses this challenge by jointly evaluating pump transfer, pump and signal propagation, and geometric feasibility before nonlinear verification. Candidate designs are subsequently assessed through analytical predictions, harmonic balance simulations, and full-wave modeling, with the evidence from each stage distinguished. For the fabricated line, the predicted pump delivery remains well below the required threshold, producing a modulation-induced transmission change of only a few hundredths of a decibel, compared with the +1 dB threshold criterion. Experimental two-tone measurements likewise provide no conclusive evidence of signal amplification under the tested conditions.

Conversely, the framework identifies a simulated design achieving an absolute input-to-output of +6.3 dB at the optimal sampled pump phase and +20 dBm pump power, within 0.09 dB of the analytical prediction. Comparison with the experimentally demonstrated amplifier of Cui et al.[48] serves as an external diagnostic benchmark. Assuming near phase matching and losses extracted from full-wave segment simulations, the analytical model predicts gain comparable to the reported results. However, incorporating the estimated phase mismatch reduces the predicted gain, highlighting the need to further verify the Bloch dispersion.

Importantly, sufficient pump delivery is a necessary design condition rather than a guarantee of amplification. The simulated design exhibits a pronounced phase-dependent response, ranging from +6.3 dB at a pump phase of 270° to −8.0 dB at 90°, compared with a pump-off transmission of −1.6 dB (Fig. 5c,d). Distinguishing stable amplification from oscillatory behavior requires additional nonlinear verification, including tests without an injected signal and at different input power levels. The proposed design satisfies these checks within the finite simulation duration. Moreover, passive evanescent modes can complicate the interpretation of Bloch eigenvalue magnitudes, reinforcing the importance of reporting absolute transmission alongside relative pump-induced gain.

Thus, we summarize three rules to follow for anyone building a time-varying transmission line with shunt varactors: (i) choose the varactor by its pump loading $\omega_p C_0$ and its depth per volt together; (ii) design stub and line jointly, so that the delivery peak meets the junction threshold inside the attenuation budgets at $2f_s$ and f_s; (iii) enforce the geometry before sampling, not after. These rules are stated for packaged varactors fed through the line; another shunt element needs its own constitutive and pump-coupling model before the same screen applies. What carries over unchanged is the question the platform was built to ask—not what the modulation is, but what the line delivers.

Methods

Platform and workflow

The workflow has three stages (Figure 1a). *Design.* The target is defined by the signal frequency f_s, the pump $f_p = 2f_s$, the varactor and bias, and the board envelope (150×30,mm). Inverse design samples stub geometries and cell counts within the envelope and evaluates each candidate using an analytical model, with four criteria of Eq. (2) applied per cell: junction transfer (A), pump transport (B), buildability (C), signal transport (D). Only candidates passing all applicable criteria proceed. *Verification.* The analytical Floquet/harmonic-ABCD core (below) gives the linear response and the parametric prediction. Circuit-level harmonic balance in ADS then resolves the varactor's nonlinear $C(V)$ at the retained harmonic orders, with the unit cell taken either from circuit elements or from a full-wave Momentum model (EM–circuit co-simulation); COMSOL frequency-domain simulations provide the independent full-wave tier for the fabricated cell. A charge-conserving time-domain (FDTD) companion on a generic RLCG line accompanies the frequency-domain models; it illustrates the mechanisms the truncated harmonic basis leaves out—the up-conversion cascade and its dispersion-assisted escape—and is not a model of any specific design. *Experiment.* The fabricated line is characterized by VNA, near-field and two-tone measurements, and its pump-off response is compared with each model tier; the two-tone results are reported with their controls. Throughout, results are labeled by tier: the analytical core *predicts*, harmonic balance *records*, and only experiment *measures*; the three are never merged into a single figure of merit, and circuit amplification records always pair the pump-on/off ratio with the absolute out/in transmission.

Analytical core and its cross-validation

To keep the analytical results physically accurate, the microstrip parameters, including the characteristic impedance Z_0 and the effective permittivity ϵ_e, are extracted from the semi-empirical Hammerstad–Jensen and Kirschning–Jansen formulations[49,50]. The tee junction between the main line and the shunt branch introduces additional parasitic effects, which are modeled with equivalent lumped capacitive and inductive elements. The ABCD matrix of each transmission-line arm, with characteristic impedance Z_0, propagation constant $\gamma = \alpha_c + j\beta$ and length $l = p/2$, is

$$M_{\mathrm{TL}} = \begin{bmatrix} \cosh\gamma l & Z_0 \sinh\gamma l \\ Z_0^{-1}\sinh\gamma l & \cosh\gamma l \end{bmatrix}. \tag{5}$$

The shunt branch, in contrast, ends in a multi-section stub, whose input impedance is obtained recursively from its termination (a grounded via or an open end) towards the varactor:

$$Z_{\mathrm{in},k} = Z_{0,k}\,\frac{Z_{\mathrm{in},k+1} + Z_{0,k}\tanh(\gamma_k l_k)}{Z_{0,k} + Z_{\mathrm{in},k+1}\tanh(\gamma_k l_k)}. \tag{6}$$

Here, $Z_{\mathrm{in},k}$ is the input impedance looking into the k-th stub section, and $Z_{0,k}$, γ_k and l_k are the characteristic impedance, propagation constant and length of that section. The input impedance of the next section towards the termination, $Z_{\mathrm{in},k+1}$, acts as the load of the k-th section. Starting from the termination impedance, the relation is applied section by section until the input impedance of the complete stub, Z_{stub}, is obtained at the varactor.

With the stub impedance known, the shunt branch of total impedance Z_{branch} (given below in Eq. (9)) enters the cell through the matrix

$$M_{\mathrm{cell}} = M_{\mathrm{TL}}\,M_{\mathrm{branch}}\,M_{\mathrm{TL}}, \qquad M_{\mathrm{branch}} = \begin{bmatrix} 1 & 0 \\ Z_{\mathrm{branch}}^{-1} & 1 \end{bmatrix}. \tag{7}$$

Since all cells are identical, the dispersion of the line can be obtained directly from M_{cell} using the Bloch–Floquet theorem[51]:

$$\cosh(\alpha + j\theta) = \tfrac{1}{2}\,(A + D), \tag{8}$$

where A and D are the diagonal elements of M_{cell}, θ is the phase factor per cell and α is the attenuation per cell of the loaded line. In a passband, α is a small dissipative residue, whereas in a stopband, it describes the spatial decay of an evanescent wave. The attenuation α therefore answers the first part of the design question, namely the transport of the pump along the line.

The second part of the design question concerns the pump that reaches the junction. Seen from the line at the tee, the full shunt branch presents the impedance

$$Z_{\text{branch}}(\omega) = R_s + j\omega L_{\text{pkg}} + \frac{1}{j\omega C_0} + Z_{\text{stub}}(\omega), \tag{9}$$

where the first three terms describe the varactor, with R_s and L_{pkg} its series resistance and package inductance and C_0 its capacitance, and Z_{stub} is the input impedance of the multi-section stub obtained above. Of the pump voltage across the whole branch, only the part that falls across C_0 modulates the junction. The branch therefore acts on the pump as a voltage divider, with transfer

$$T(f) \;=\; \left| \frac{Z_C}{Z_{\text{pkg}} + Z_C + Z_{\text{stub}}} \right|, \qquad Z_C = \frac{1}{j\omega C_0}, \quad Z_{\text{pkg}} = R_s + j\omega L_{\text{pkg}}. \tag{10}$$

Together, α and T describe the complete delivery chain shown on the left of Fig. 2a, in which the pump decays by α per cell along the line and reaches each junction through T.

Once delivered, the pump modulates the junction, and the capacitive term $1/(j\omega C_0)$ of Eq. (9) becomes time-dependent. This term is conveniently described through the elastance $S = 1/C$, with static value $S_0 = 1/C_0$ (Fig. 2a, centre),

$$S(t) = S_0 + \Delta S \cos(\omega_m t + \varphi), \qquad 0 \le \Delta S \le S_0, \tag{11}$$

where the modulation amplitude ΔS is set by the delivered pump voltage. The elastance representation is chosen because it makes the charge dynamics linear with periodic coefficients. For a real harmonic drive $v(t) = \text{Re}[V_0 e^{j\omega_s t}]$, the junction charge obeys the driven Hill equation with a periodically varying coefficient:

$$L\ddot{Q}(t) + R\dot{Q}(t) + \big[S_0 + \Delta S \cos(\omega_m t + \varphi)\big] Q(t) = \text{Re}\big[V_0 e^{j\omega_s t}\big], \tag{12}$$

with $R = R_s$ and $L = L_{\text{pkg}}$ the series elements of the branch. where $R = R_s$ and $L = L_{\text{pkg}}$. Because the modulation repeats in time, the charge contains not only the signal frequency f_s but also copies of it shifted by multiples of the pump frequency, at $-3f_s$, $-f_s$ (the idler), $3f_s$, $5f_s$ and so on. This Floquet expansion, $Q(t) = \sum_n Q_n e^{j(\omega_s + n\omega_m)t}$, turns Eq. (12) into a chain of equations for the amplitudes Q_n, in which each harmonic is coupled only to its two neighbors (Fig. 2a, right),

$$\begin{aligned} &\frac{\Delta S e^{+j\varphi}}{2} Q_{n-1} + \Big[S_0 + jR\,\omega_n - L\,\omega_n^2\Big] Q_n + \frac{\Delta S e^{-j\varphi}}{2} Q_{n+1} = \tfrac{1}{2}\big(V_0\,\delta_{n0} + V_0^*\,\delta_{n,-1}\big), \\ &\omega_n = \omega_s + n\omega_m, \qquad \omega_m = 2\omega_s. \end{aligned} \tag{13}$$

The two parts of this system have a clear physical origin. The diagonal terms are $j\omega_n$ times the branch impedance at each harmonic (the stub adds $j\omega_n Z_{\text{stub}}$), so they are fixed by the passive branch. The off-diagonal terms $\frac{1}{2}\Delta S e^{\mp j\varphi}$ represent the parametric coupling between neighboring harmonics, so they are fixed by the delivered pump. The branch communicates with the line through its current spectrum $I(\omega) = \sum_n j\omega_n Q_n\,\delta(\omega - \omega_n)$. Truncated to $\pm f_s$ and $\pm 3f_s$ and embedded in the harmonic-ABCD cascade, this system forms the platform's analytical core. Its two independent formulations agree to a residual of 1.8×10^{-16}. Because a real signal contains both $+f_s$ and $-f_s$, which share one Floquet ladder when $f_p = 2f_s$, even a single driven branch responds as $A_{\text{out}} = H_s A_{\text{in}} + H_i e^{j\varphi} A_{\text{in}}^*$ and is therefore phase sensitive. The core thus predicts a single bounded gain lobe whose maximum and minimum are separated by exactly 180° in pump phase (Supplementary Section S2).

FDTD companion (charge form)

The time-domain simulations were performed with the FDTD method applied to an RLCG transmission-line model. The current was updated by the standard staggered scheme[52,53] the voltage with the charge-conserving scheme of Eq. (15). The line was divided into cells of $\Delta z = 0.667\,\mathrm{mm}$ (30 points per wavelength at 15 GHz), and the time step was $\Delta t = \Delta z/(2c_0) = 1.11\,\mathrm{ps}$. With this grid, one wavelength on the line at the signal frequency $f_s = 3\,\mathrm{GHz}$ contains about 92 points. Both ends of the line were terminated with absorbing boundaries, and the line was excited by a Gaussian pulse. For a time-varying shunt capacitance, the node equation of the telegrapher system has to conserve charge,

$$-\frac{\partial i}{\partial z} \;=\; Gv + \frac{\partial}{\partial t}\big[C(z,t)\,v\big] \;=\; C\frac{\partial v}{\partial t} + v\frac{\partial C}{\partial t} + Gv. \tag{14}$$

The term $v\,\partial_t C$ is required by the energy balance, since through it the modulation exchanges the power $\frac{1}{2}\dot{C}v^2$ with the line (Supplementary Section S1). The discrete update therefore advances the charge $q = Cv$ rather than the voltage,

$$q_k^{n+1} = q_k^n - \Delta t\left[\frac{i_{k+1/2}^{\,n+1/2} - i_{k-1/2}^{\,n+1/2}}{\Delta z} + G v_k^n\right], \qquad v_k^{n+1} = q_k^{n+1}/\,C_k^{n+1}, \tag{15}$$

with the modulation prescribed as $S(t) = S_0[1 + m\sin(2\pi f_m t)]$, $C = 1/S$ (Methods). The term is not a small correction: omitting it changes the pump-on/off ratio by 0.50–0.56 dB at $m = 0.5$ over two and four wavelengths (Supplementary Section S4).

Circuit-level simulation and certification (ADS)

The transmission line is modeled in ADS using MLIN, MTEE, MLEF, and VIAGND elements on a Rogers RO4003C substrate. The SMV1245-079LF varactors are represented by a SPICE capacitance model with $C_0 = 7.37$ pF, $R_s = 2.0\,\Omega$, and $L_{\mathrm{pkg}} = 0.7$ nH. Harmonic balance simulations include degenerate mixing products satisfying $m + 2n = 1$, with absolute input to output gain referenced to the nominal available signal power. Nonconvergent solutions are classified as unresolved.

Certification requires a bounded pump phase response, an off state ratio $r_A < 0.5$, an input scaling slope ≥ 0.5, convergence at all sampled phases, and analytical agreement within $\varepsilon \leq 5$ dB. For the certified design, ADS Momentum simulations cover 0.5 to 20 GHz using a six port unit cell and an additional diagnostic port to evaluate junction pump transfer. The SMV2019-079LF varactor is modeled using its native ADS SPICE representation with package parasitics and bias circuitry.

The design search spans $f_s = 0.5$ to 2.8 GHz, up to 40 cells, and line lengths of 300 mm, subject to pump delivery, attenuation, phase, and geometric constraints. Harmonic balance simulations use $f_s = 1.262702$ GHz at -40 dBm, with a pump at $2f_s$ applied through the same $50\,\Omega$ port. The pump is increased in 1 dB steps, and its phase is sampled every 45° using harmonic order 7. Tolerance analysis and finite duration stability checks are detailed in Supplementary Table S2.

Full-wave simulation (COMSOL)

The simulated scattering parameters were obtained using the frequency-domain solver of COMSOL Multiphysics. The microstrip transmission line was modeled on a dielectric substrate with a relative permittivity of 3.38, including substrate loss, and enclosed by open (radiation) boundaries. The metallic parts were assigned as perfect electric conductors (PEC) and excitation and termination were implemented through transverse electromagnetic (TEM) wave ports. A lumped RLC element was used to represent the varactor diode, with an effective area matching the physical dimensions of the diode. The element parameters were set to R=1.5 Ohm, L=1.7 nH, and C=7

pF in a series configuration. The overall geometry of the model and the boundary configuration reproduced the physical prototype configuration used in the experiments. The unit cell dispersion was obtained separately from an eigenmode analysis with Floquet boundary conditions.

Fabrication

The prototype is fabricated on Rogers RO4003C ($\varepsilon_r = 3.38$, $\tan\delta \approx 0.0027$, thickness 1.54 mm) with board dimensions of $150 \times 30\,\mathrm{mm}^2$. The PCB layout follows the simulated structure, with identical microstrip dimensions and 20 varactor-loaded unit cells. The top conductor is connected to the ground plane through two plated through-holes, each with a radius of 0.8 mm.

Measurements

Pump-off scattering parameters were measured from 0.01 to 20 GHz with a Rohde & Schwarz vector network analyser (VNA). In the two tone experiments, the signal and the pump were generated by the two output channels of a Keysight M9384B VXG signal generator. The two tones were combined in a Marki Microwave C−0265 directional coupler and injected into the input port of the line. Transmitted spectrum was recorded with a Rohde & Schwarz FSW signal and spectrum analyser.

Near-field scans were performed with a monopole probe mounted on an XY translation stage driven by a stepper motor. The sample was placed horizontally, with the probe approximately 1.5 mm above its surface over the whole scanning range. The line was excited at one end through an SMA connector, and the opposite end was terminated with a 50 Ω load. Maps of the complex E_z field and of the power intensity were recorded along the line with a spatial resolution of 0.5 mm. The near-field scans were carried out in both the unmodulated and the modulated regime. For these scans, the signal and pump tones were generated by two Agilent signal generators (E8257D-520 and E8257D-540), combined in a directional coupler, and fed to the line through a coaxial cable. In the unmodulated regime, only the signal tone was applied. In the modulated regime, both tones were applied simultaneously. The transmitted spectrum was recorded with an signal analyser.

Open toolchain and evidence tiers

The toolchain comprises the analytical core, optimizer with a delivery-screening stage, ADS bridge and circuit certification pipeline, and figure generators; the FDTD results come from a separate time-domain companion code (data deposit, `runs/fdtd_companion_v3/`).

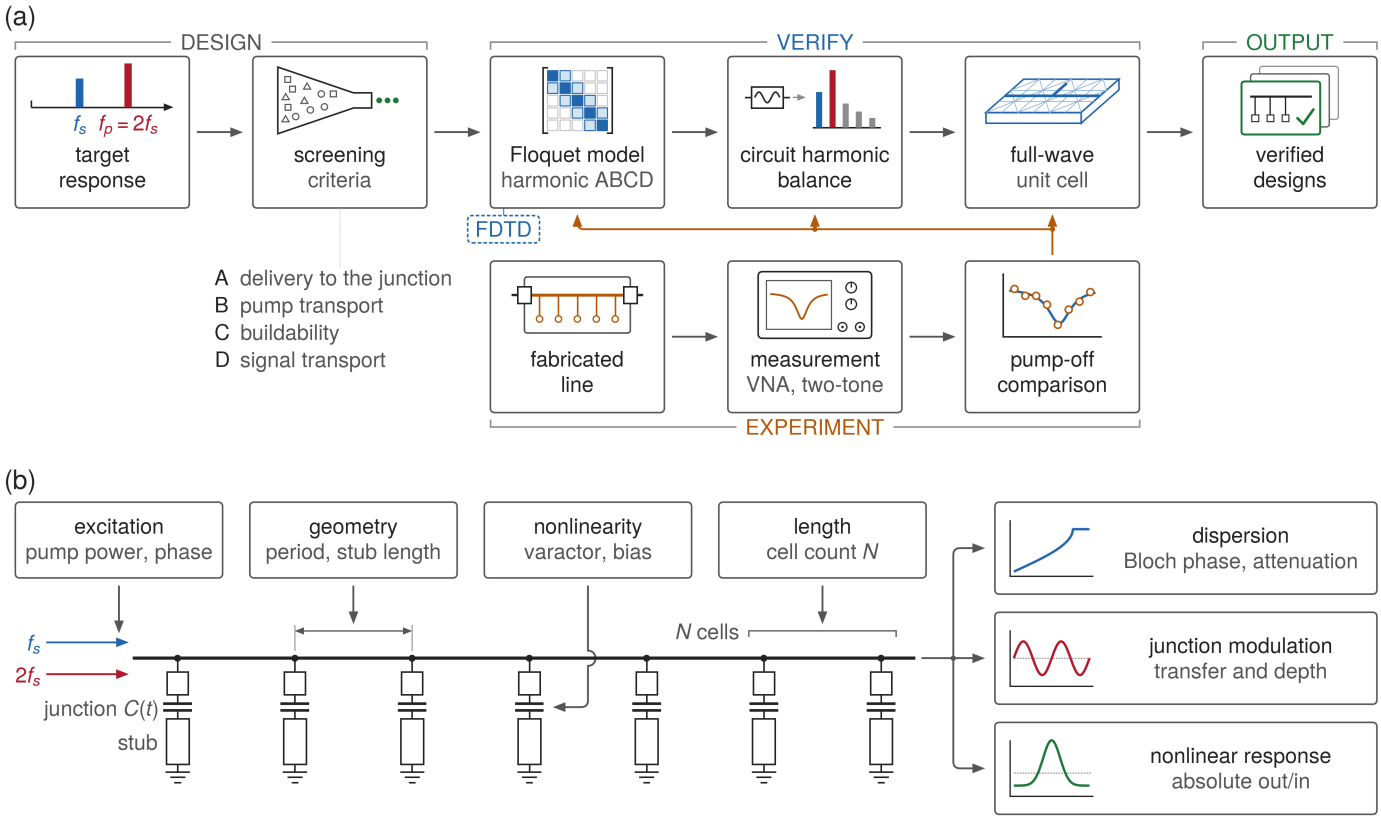


Figure 1: Design strategy and physical platform for time-varying transmission lines. (a) The design framework in three stages. Design: the target is set by the signal frequency f_s, the degenerate pump $f_p = 2f_s$, the response class and component constraints; candidates are screened against four criteria—pump delivery to the junction (A), pump transport along the line (B), buildability (C) and signal transport (D). Verification: the analytical Floquet/harmonic-ABCD core gives the first estimate of the linear and parametric response, followed by circuit-level harmonic balance (ADS) and full-wave simulation of the unit cell (COMSOL, Momentum) with EM–circuit co-simulation; a charge-conserving FDTD companion on a generic line illustrates the time-domain mechanisms the truncated core leaves out. Experiment: VNA, near-field and two-tone measurements of the fabricated 20-cell SMV1245 line are compared with each model tier. **(b)** The TVTL: a microstrip line with N periodic cells loaded by varactor stubs of time-varying capacitance $C(t)$. Signal (f_s) and pump ($f_p = 2f_s$) enter through a common port; the transmitted response is recorded at the opposite port. The pump propagates along the loaded line according to its Bloch dispersion and reaches the junction through the varactor package and the stub (Fig. 2a). Four parameter groups—excitation, geometry, nonlinearity and length—jointly determine three coupled responses: dispersion (Bloch phase and attenuation), modulation at the junction (pump transfer and depth), and the nonlinear response (absolute output-to-input transmission).

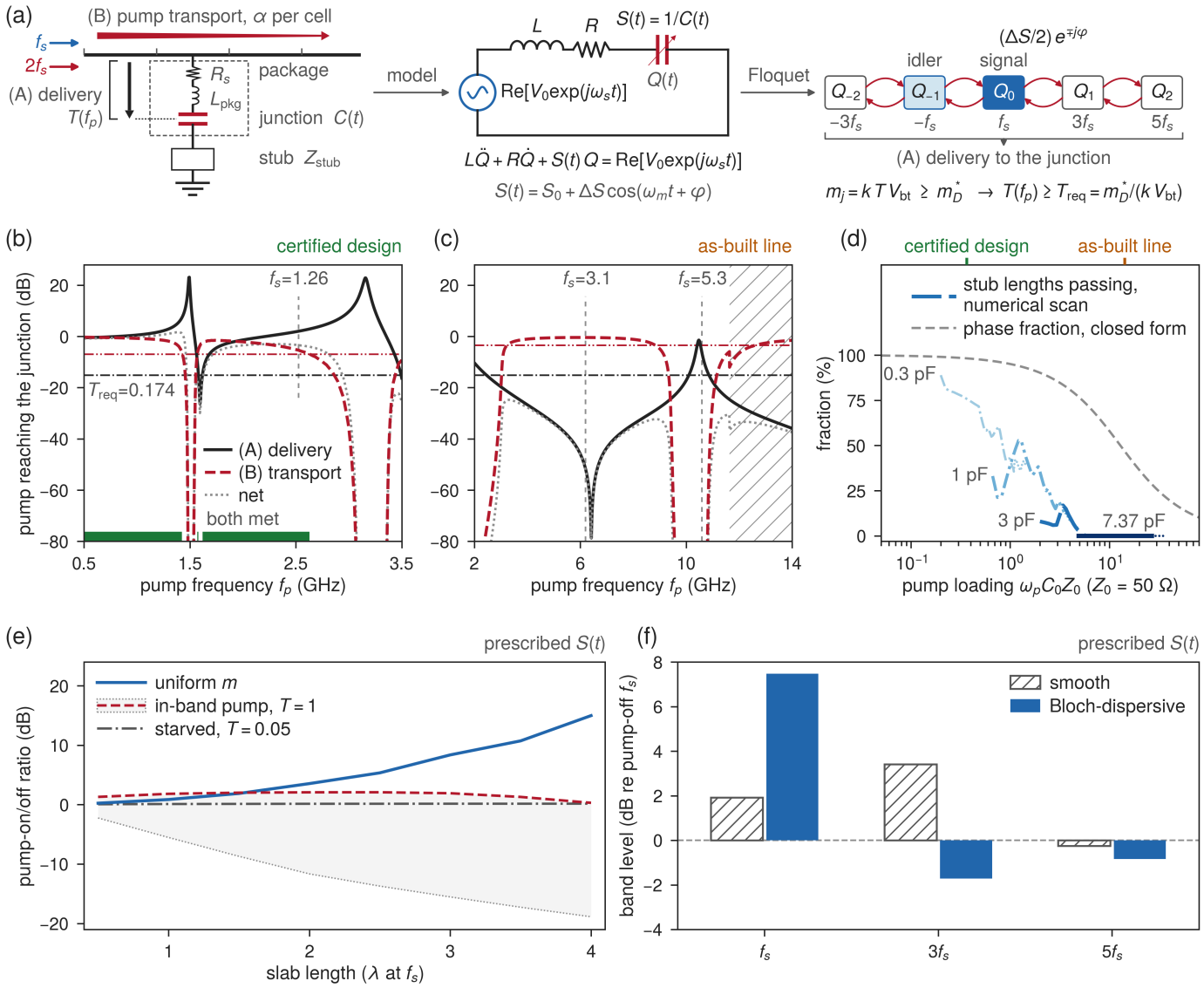


Figure 2: Pump delivery and the time-domain response. **(a)** Delivery chain and branch model: signal (f_s) and pump ($2f_s$) enter from the left; the pump decays by α per cell (transport, B) and reaches each junction $C(t)$ through the package (R_s, L_{pkg}) and stub Z_{stub} with transfer $T(f_p)$ (delivery, A). Center: the branch as a series L–R circuit with elastance $S(t) = 1/C(t)$ (Hill equation); right: its Floquet harmonics Q_n, which set the threshold $T_{\mathrm{req}} = m_D^*/(kV_{\mathrm{bt}})$ (Methods). **(b, c)** Pump level at the junction versus pump frequency for the certified design (b; SMV2019, 40 cells, 8.7,V) and the as-built line (c; SMV1245, 20 cells, 0,V): delivery $20\log_{10} T$ (black), transport loss $-8.686\,N\alpha$ (red dashed), their sum (grey dotted); thresholds $T_{\mathrm{req}} = 0.174$ and $\alpha_{\max} = 0.02$,Np/cell over N cells (dash-dotted); operating $2f_s$ (vertical dashed); green bars: both met. **(d)** Fraction of stub lengths (0.4–3.0 times the as-built stub) meeting A and B versus pump loading $\omega_p C_0 Z_0$; one curve per C_0 (0.3, 1, 3, 7.37,pF), one point per pump frequency (2–16,GHz). **(e)** FDTD pump-on/off ratio at f_s versus line length: uniform modulation of depth m (blue); in-band pump with $T = 1$ at its best phase (red dashed; shading: all phases); the same with $T = 0.05$ (dash-dotted). **(f)** Output at f_s, $3f_s$, $5f_s$ relative to the pump-off signal, best phase, three wavelengths: smooth line (hatched) and Bloch-loaded line with $3f_s$ in its stopband (blue).

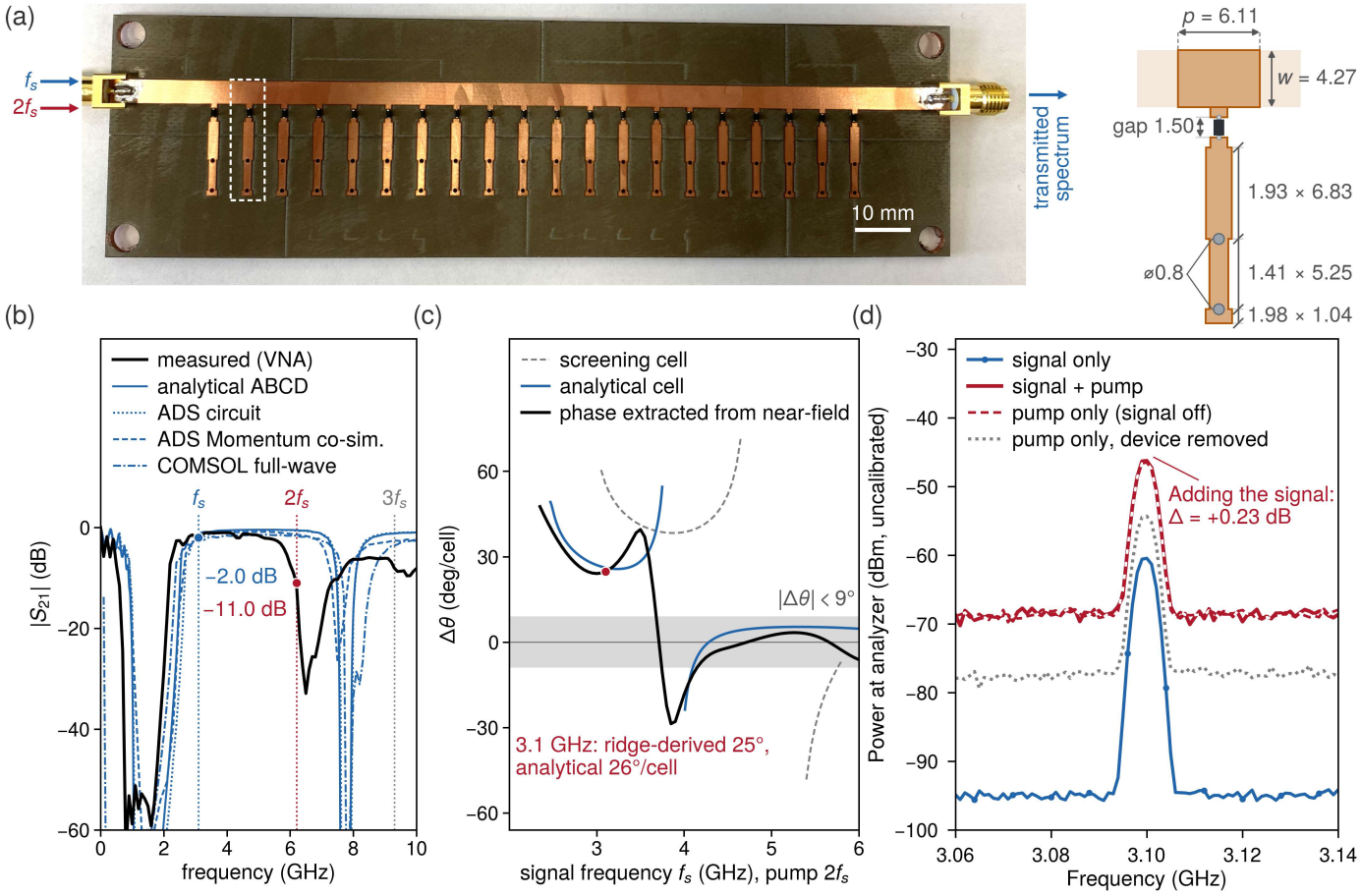


Figure 3: The fabricated line: specimen, pump-off response, and two-tone control. **(a)** Photograph of the fabricated board (RO4003C, 152.7×42.7 mm) with 20 unbiased SMV1245 cells, taken before the varactors were soldered. The signal (f_s) and pump ($2f_s$) are injected at the left connector, and the transmitted spectrum is recorded at the right connector. The dashed frame marks one unit cell, shown enlarged on the right with its dimensions in mm, including the two 0.8 mm holes for the ground connections. **(b)** Transmission coefficient $|S_{21}|$ of the line without pump, measured by VNA and computed by four models: analytical ABCD, ADS circuit, ADS Momentum co-simulation, and COMSOL full-wave. Vertical dotted lines mark f_s, $2f_s$ and $3f_s$, and the dots give the measured values at f_s and $2f_s$. **(c)** Pump phase mismatch per cell, $\Delta\theta = \theta(2f_s) - 2\theta(f_s)$, as a function of signal frequency, extracted from the near-field scan and computed for the analytical and screening cells. The shaded band marks $|\Delta\theta| < 180°/N$, and the dot marks 3.1 GHz. **(d)** Two-tone spectra around $f_s = 3.1$ GHz with the pump at 6.2 GHz, recorded for the signal only, the signal and pump together, the pump only, and the pump only with the device removed. The annotation gives the change in the pump-on line when the signal is added.

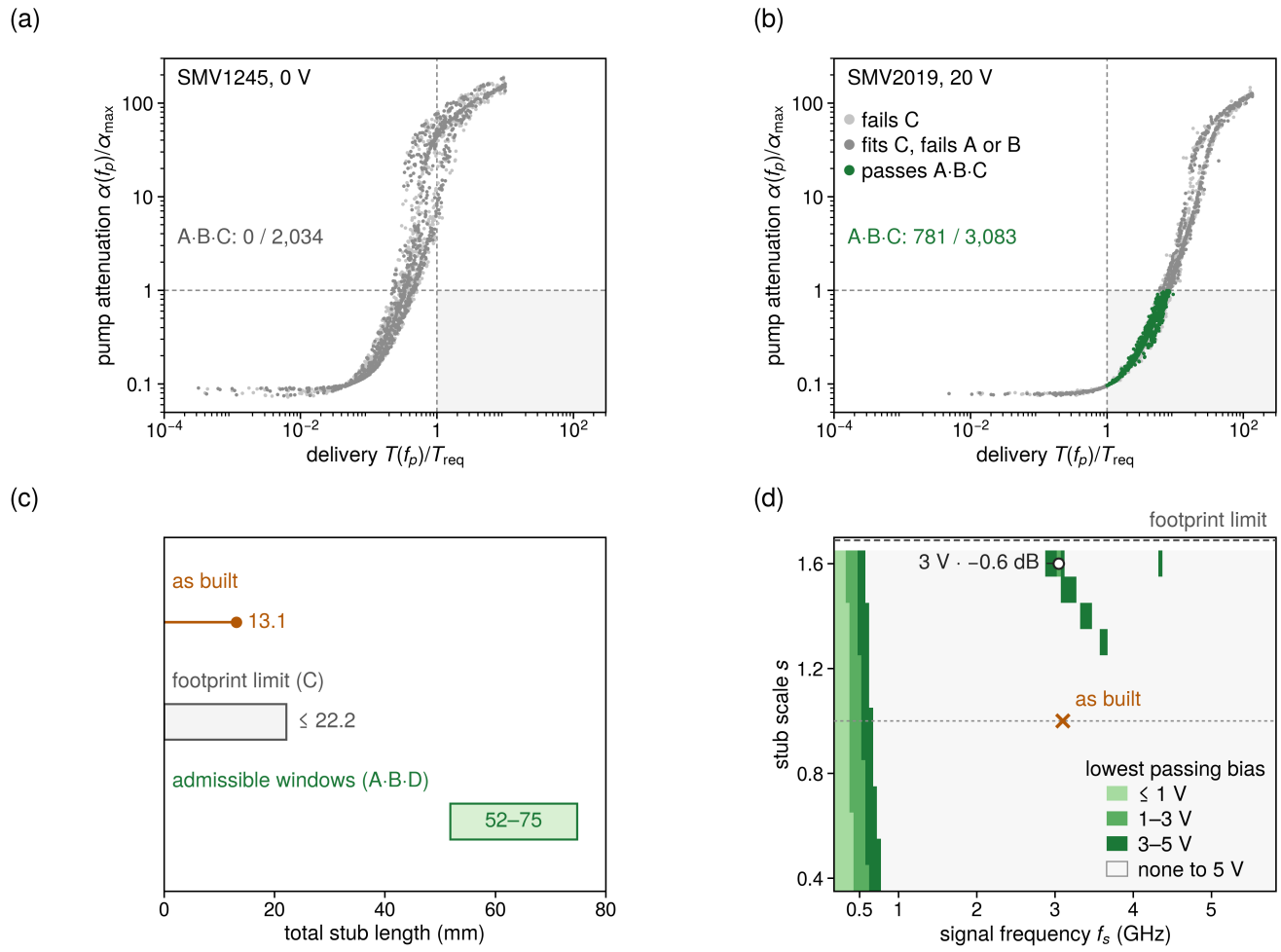


Figure 4: The cost of the rule and its constructive use. Two varactors are compared: the SMV1245 at 0 V, used in the fabricated line, and the SMV2019 at 20 V. Candidate designs are screened against four criteria: delivery of the pump to the junction (A), transport of the pump along the line (B), buildability within the 150×30 mm footprint (C), and transport of the signal (D). **(a, b)** Pump attenuation $\alpha(f_p)/\alpha_{max}$ versus delivery $T(f_p)/T_{req}$ at $f_s = 3.1$ GHz ($N_{model} = 15$), for the first (a) and second (b) varactor. Each point is one design. The dashed lines at 1 mark the thresholds $T_{req} = 0.174$ and $\alpha_{max} = 0.02$ Np/cell, and the shaded lower-right region contains the designs meeting both A and B. Light grey points fail C, dark grey points fit C but fail A or B, and green points pass all three. The label in each panel reads as passing designs / evaluated designs. **(c)** Stub lengths allowed by buildability compared with those required by the electrical criteria. The orange line marks the stub of the fabricated line, the grey box the range allowed by the footprint limit (C), and the green box the admissible windows meeting A, B and D. **(d)** Lowest reverse bias at which a buildable cell of the fabricated line meets A, B and D. The map is plotted over signal frequency f_s and stub scale s, the stub length relative to the as-built stub. Green shades give the lowest passing bias. Grey means that no bias up to 5 V is sufficient. The dashed line marks the footprint limit (C). The dotted line and cross mark the as-built design. The circle marks an example point (Supplementary Table S3), labelled with its bias and its out/in transmission at +10 dBm.

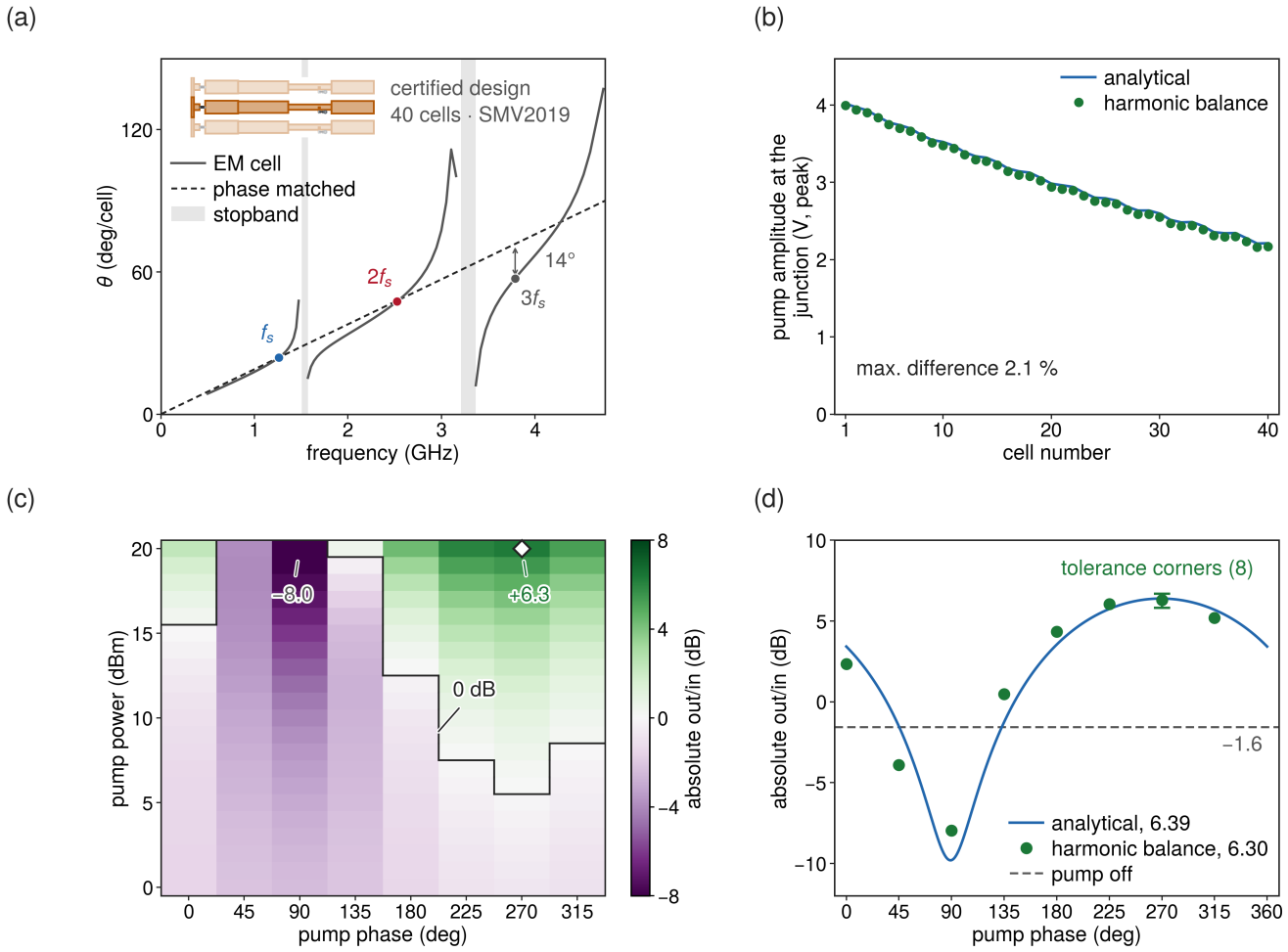


Figure 5: The certified design: prediction and record. The design uses SMV2019 varactors in 40 cells (237 mm) at 8.7 V bias, with the signal at 1.26 GHz and the pump at $2f_s$ and +20 dBm. All results are simulations. **(a)** Phase advance per cell of the EM-modeled cell versus frequency, showing which frequencies are phase matched. The solid curve is the pump-off Bloch phase, the dashed line the phase-matching condition, and the grey bands the stopbands. The dots mark f_s, $2f_s$ and $3f_s$; the arrow gives the 14° mismatch at $3f_s$. Inset: three cells drawn to scale. **(b)** Pump amplitude at the junction of each of the 40 cells, showing how the pump decays along the line. The line is the analytical prediction and the points are harmonic-balance results. **(c)** Absolute out/in transmission versus pump phase and pump power, from harmonic balance on a 45° × 1 dB grid. The black contour marks 0 dB. The diamond marks the certified point (270°, +20 dBm), and the labels give the maximum and minimum values. **(d)** Absolute out/in transmission versus pump phase at +20 dBm pump, comparing prediction and simulation. The line is the analytical prediction and the points are harmonic-balance results, with their peak values in the legend. The error bar at 270° shows the spread over the nominal design and eight tolerance corners. The dashed line gives the pump-off level.

References

[1] Galiffi, E. *et al.* Photonics of time-varying media. *Adv. Photonics* **4**, 014002 (2022). https://doi.org/10.1117/1.ap.4.1.014002.

[2] Caloz, C. & Deck-Léger, Z.-L. Spacetime metamaterials—part I: general concepts. *IEEE Trans. Antennas Propag.* **68**, 1569–1582 (2020). https://doi.org/10.1109/tap.2019.2944225.

[3] Caloz, C. & Deck-Léger, Z.-L. Spacetime metamaterials—part II: theory and applications. *IEEE Trans. Antennas Propag.* **68**, 1583–1598 (2020). https://doi.org/10.1109/tap.2019.2944216.

[4] Pacheco-Peña, V., Solís, D. M. & Engheta, N. Time-varying electromagnetic media: opinion. *Opt. Mater. Express* **12**, 3829–3836 (2022). https://doi.org/10.1364/ome.471007.

[5] Lemoult, F., Kaina, N., Fink, M. & Lerosey, G. Wave propagation control at the deep subwavelength scale in metamaterials. *Nat. Phys.* **9**, 55–60 (2013). https://doi.org/10.1038/nphys2480.

[6] Gaikwad, C., Kowsari, D., Chen, W. & Murch, K. Observing parity-time symmetry breaking in a Josephson parametric amplifier. *Phys. Rev. Res.* **5**, L042024 (2023). https://doi.org/10.1103/physrevresearch.5.l042024.

[7] Li, H., Moussa, H., Sounas, D. & Alù, A. Parity-time symmetry based on time modulation. *Phys. Rev. Appl.* **14**, 031002 (2020). https://doi.org/10.1103/physrevapplied.14.031002.

[8] Taravati, S. & Caloz, C. Mixer-duplexer-antenna leaky-wave system based on periodic space-time modulation. *IEEE Trans. Antennas Propag.* **65**, 442–452 (2017). https://doi.org/10.1109/tap.2016.2632735.

[9] Hadad, Y., Soric, J. & Alù, A. Breaking temporal symmetries for emission and absorption. *Proc. Natl. Acad. Sci. USA* **113**, 3471–3475 (2016). https://doi.org/10.1073/pnas.1517363113.

[10] Qin, S., Xu, Q. & Wang, Y. E. Nonreciprocal components with distributedly modulated capacitors. *IEEE Trans. Microw. Theory Tech.* **62**, 2260–2272 (2014). https://doi.org/10.1109/tmtt.2014.2347935.

[11] Qin, S. & Wang, Y. E. A nonreciprocal, frequency-tunable notch amplifier based on distributedly modulated capacitors (DMC). In *IEEE MTT-S Int. Microwave Symp. Dig.*, 1–3 (2016). https://doi.org/10.1109/mwsym.2016.7540316.

[12] Taravati, S. & Caloz, C. Space-time modulated nonreciprocal mixing, amplifying and scanning leaky-wave antenna system. In *2015 IEEE International Symposium on Antennas and Propagation & USNC/URSI National Radio Science Meeting*, 639–640 (2015). https://doi.org/10.1109/APS.2015.7304706.

[13] Taravati, S. & Kishk, A. A. Space-time modulation: principles and applications. *IEEE Microw. Mag.* **21**, 30–56 (2020). https://doi.org/10.1109/mmm.2019.2963606.

[14] Tamir, T., Wang, H. C. & Oliner, A. A. Wave propagation in sinusoidally stratified dielectric media. *IEEE Trans. Microw. Theory Tech.* **12**, 323–335 (1964). https://doi.org/10.1109/tmtt.1964.1125815.

[15] Cassedy, E. S. Dispersion relations in time-space periodic media part II—unstable interactions. *Proc. IEEE* **55**, 1154–1168 (1967). https://doi.org/10.1109/proc.1967.5775.

[16] Liu, X. & McNamara, D. A. The use of the FDTD method for electromagnetic analysis in the presence of independently time-varying media. *Int. J. Infrared Millim. Waves* **28**, 759–778 (2007). https://doi.org/10.1007/s10762-007-9251-7.

[17] Shao, J., Ma, X., Kang, Z. & Wang, J. Numerical treatment for electromagnetic wave in time-variant medium using generalized PITD method. *IEEE Microw. Wirel. Compon. Lett.* **30**, 4–7 (2020). https://doi.org/10.1109/lmwc.2019.2952012.

[18] Kumar, A., Dash, J. C. & Sarkar, D. FDTD analysis of transmission line loaded with time-varying shunt capacitors for mixer applications. In *IEEE CONECCT*, 1–6 (2022). https://doi.org/10.1109/conecct55679.2022.9865819.

[19] Kumar, A. & Sarkar, D. FDTD analysis of space-time metamaterials using modulated TVTLs for frequency translation, mixing and non-reciprocity. In *Proc. 53rd Eur. Microwave Conf.*, 311–314 (2023). https://doi.org/10.23919/eumc58039.2023.10290288.

[20] Sarkar, D. *FDTD Analysis of Guided Electromagnetic Wave Interaction with Time-Modulated Dielectric Medium* (Springer, Singapore, 2022). https://doi.org/10.1007/978-981-19-1630-4.

[21] Koutserimpas, T., Alù, A. & Fleury, R. Parametric amplification and bidirectional invisibility in $\mathcal{PT}$-symmetric time-Floquet systems. *Phys. Rev. A* **97**, 013839 (2018). https://doi.org/10.1103/physreva.97.013839.

[22] Mirmoosa, M. S., Ptitcyn, G., Asadchy, V. S. & Tretyakov, S. A. Time-varying reactive elements for extreme accumulation of electromagnetic energy. *Phys. Rev. Appl.* **11**, 014024 (2019). https://doi.org/10.1103/PhysRevApplied.11.014024.

[23] Asgari, M. M., Garg, P., Wang, X., Mirmoosa, M. S., Rockstuhl, C. & Asadchy, V. Theory and applications of photonic time crystals: a tutorial. *Adv. Opt. Photon.* **16**, 958–1063 (2024). https://doi.org/10.1364/AOP.525163.

[24] Martínez-Romero, J. S. & Halevi, P. Parametric resonances in a temporal photonic crystal slab. *Phys. Rev. A* **98**, 053852 (2018). https://doi.org/10.1103/physreva.98.053852.

[25] Cullen, A. L. A travelling-wave parametric amplifier. *Nature* **181**, 332 (1958). https://doi.org/10.1038/181332a0.

[26] Tien, P. K. Parametric amplification and frequency mixing in propagating circuits. *J. Appl. Phys.* **29**, 1347–1357 (1958). https://doi.org/10.1063/1.1723440.

[27] Louisell, W. H. *Coupled Mode and Parametric Electronics* (Wiley, New York, 1960).

[28] Landauer, R. Shock waves in nonlinear transmission lines and their effect on parametric amplification. *IBM J. Res. Dev.* **4**, 391–401 (1960). https://doi.org/10.1147/rd.44.0391.

[29] Ho Eom, B., Day, P. K., LeDuc, H. G. & Zmuidzinas, J. A wideband, low-noise superconducting amplifier with high dynamic range. *Nat. Phys.* **8**, 623–627 (2012). https://doi.org/10.1038/nphys2356.

[30] Macklin, C. *et al.* A near-quantum-limited Josephson traveling-wave parametric amplifier. *Science* **350**, 307–310 (2015). https://doi.org/10.1126/science.aaa8525.

[31] Planat, L. *et al.* Photonic-crystal Josephson traveling-wave parametric amplifier. *Phys. Rev. X* **10**, 021021 (2020). https://doi.org/10.1103/physrevx.10.021021.

[32] Kozyrev, A. B., Kim, H. & van der Weide, D. W. Parametric amplification in left-handed transmission-line media. *Appl. Phys. Lett.* **88**, 264101 (2006). https://doi.org/10.1063/1.2214136.

[33] Kozyrev, A. B. & van der Weide, D. W. Nonlinear wave propagation phenomena in left-handed transmission-line media. *IEEE Trans. Microw. Theory Tech.* **53**, 238–245 (2005). https://doi.org/10.1109/tmtt.2004.839305.

[34] Zou, X. Monolithically integrated time-varying transmission lines (TVTL) for tunable and interference resilient RF front ends. PhD thesis, University of California, Los Angeles (2021). https://escholarship.org/uc/item/2mt0q949.

[35] Dai, W., Liu, G., Joshi, V., Miano, A., Sivak, V., Shankar, S. & Devoret, M. H. Optimizing the pump coupling for a three-wave mixing Josephson parametric amplifier. *Phys. Rev. Appl.* **23**, 054069 (2025). https://doi.org/10.1103/PhysRevApplied.23.054069.

[36] Malnou, M. Artificial transmission line synthesis tailored for traveling-wave parametric processes. Preprint at https://arxiv.org/abs/2510.24753 (2026).

[37] Denney, C., Genter, K., Cicak, K., Teufel, J. D., Aumentado, J., Lecocq, F. & Malnou, M. A traveling-wave parametric amplifier with integrated diplexers. Preprint at https://arxiv.org/abs/2603.12327 (2026).

[38] English, L. Q. *et al.* Generation of localized modes in an electrical lattice using subharmonic driving. *Phys. Rev. Lett.* **108**, 084101 (2012). https://doi.org/10.1103/physrevlett.108.084101.

[39] Gorkunov, M. V. & Lapine, M. Tuning of a nonlinear metamaterial band gap by an external magnetic field. *Phys. Rev. B* **70**, 235109 (2004). https://doi.org/10.1103/physrevb.70.235109.

[40] Lee, W. & Afshari, E. Distributed parametric resonator: a passive CMOS frequency divider. *IEEE J. Solid-State Circuits* **45**, 1834–1844 (2010). https://doi.org/10.1109/jssc.2010.2056833.

[41] Zou, X. *Parametric Amplification of Time-Varying Transmission Lines (TVTL) and its Applications*. M.S. thesis, University of California, Los Angeles (2018).

[42] Huang, B., Zhu, Z., Yu, G. & Gao, Z. Observation of full momentum bandgap in photonic time crystals. Preprint at https://arxiv.org/abs/2604.17408 (2026).

[43] Xiong, J. *et al.* Observation of wave amplification and temporal topological state in a non-synthetic photonic time crystal. *Nat. Commun.* **16**, 11182 (2025). https://doi.org/10.1038/s41467-025-66154-4.

[44] Jones, T. R., Prokopeva, L. J., Kildishev, A. V., Segev, M. & Peroulis, D. Demonstration of Broadband Non-Resonant Time-Crystal Amplification in Microwaves. Preprint at https://arxiv.org/abs/2605.21014 (2026).

[45] Kovalev, F. V. & Shadrivov, I. V. Parametric metasurfaces for amplified up-conversion of electromagnetic waves. *Appl. Phys. Lett.* **126**, 261702 (2025). https://doi.org/10.1063/5.0270946.

[46] Kovalev, F., Maslovski, S., Abraray, A. & Shadrivov, I. Amplified up-conversion of electromagnetic waves using time-varying metasurfaces. Preprint at https://arxiv.org/abs/2602.08193v2 (2026).

[47] Pacheco-Peña, V., Kiasat, Y., Solís, D. M., Edwards, B. & Engheta, N. Holding and amplifying electromagnetic waves with temporal non-foster metastructures. *Nat. Commun.* **16**, 2757 (2025). https://doi.org/10.1038/s41467-025-57739-0.

[48] Cui, W. Y., Zhang, J., Luo, Y., Gao, X. & Cui, T. J. Dynamic switching from coherent perfect absorption to parametric amplification in a nonlinear spoof plasmonic waveguide. *Nat. Commun.* **15**, 2824 (2024). https://doi.org/10.1038/s41467-024-47191-x.

[49] Hammerstad, E. & Jensen, O. Accurate models for microstrip computer-aided design. In *IEEE MTT-S Int. Microwave Symp. Dig.*, 407–409 (1980). https://doi.org/10.1109/mwsym.1980.1124303.

[50] Kirschning, M. & Jansen, R. H. Accurate model for effective dielectric constant of microstrip with validity up to millimetre-wave frequencies. *Electron. Lett.* **18**, 272–273 (1982). https://doi.org/10.1049/el:19820186.

[51] Pozar, D. M. *Microwave Engineering* 4th edn (Wiley, Hoboken, 2012).

[52] Yee, K. S. Numerical solution of initial boundary value problems involving Maxwell's equations in isotropic media. *IEEE Trans. Antennas Propag.* **14**, 302–307 (1966). https://doi.org/10.1109/tap.1966.1138693.

[53] Taflove, A. & Hagness, S. C. *Computational Electrodynamics: The Finite-Difference Time-Domain Method* (Artech House, Norwood, 2005).

[54] Abzaliyeva, A., Valagiannopoulos, C. & Orazbayev, B. floquet-line-design: physics-guided design and verification of time-varying transmission lines, version v1.0.3-paper. *Zenodo* (2026). https://doi.org/10.5281/zenodo.23585014.

Data availability

The data supporting this study's findings are openly available in the Zenodo repository at https://doi.org/10.5281/zenodo.23561779. The record contains the harmonic-balance and analytical records of the certified design and of the design campaign (including the 168-point pump-phase/pump-power map and the tolerance corners), the screening scans behind Figs. 2 and 4, the passive model tiers and the VNA, near-field and two-tone measurement records of the fabricated line, the time-domain companion runs (current engine and the withdrawn earlier runs, marked as such), and the figure records of the submitted figure pack with the index of every number quoted in the paper and its source file. A README maps each figure, table, and quoted value to its file.

Code availability

The analysis and design code (`floquet-line-design`, release `v1.0.3-paper`) is openly available at https://github.com/wavelabnu/floquet-line-design and archived at https://doi.org/10.5281/zenodo.23585014 under the BSD-3-Clause license. The release contains the Floquet/harmonic-ABCD core, the screening rule, the inverse-design and certification pipeline with its ADS harmonic-balance bridge, the time-domain companion, the figure generators, and the test suite that reproduces the certified record (`r17b_reproduce`). ADS and COMSOL are commercial tools; the decks and model files used are included in the data record.

Funding statement

This research was funded by the Science Committee of the Ministry of Science and Higher Education of the Republic of Kazakhstan (Grant No. AP26195569), by Nazarbayev University under FDCRGP no 040225FD4719 and 201223FD2606.

Author contributions

A.A. carried out platform development, ran the optimizer/ADS campaigns, provided fabrication support, performed measurements, conducted near-field scans, and performed FDTD simulations; C.V. developed the elastance/Floquet analytical formulation of the modulated unit cell; B.O. conceived the study and supervised the work. All authors contributed to the writing of the manuscript.

Competing interests

The authors declare no competing interests.

Additional information

Supplementary Information accompanies this paper (Supplementary Sections S1–S9, Figs. S1–S17, Tables S1–S8).

Supplementary Files

This is a list of supplementary files associated with this preprint. Click to download.

- TVTLSM.pdf